Electron spin inversion in fluorinated graphene nanoribbons

Bartłomiej Rzeszotarski, Alina Mreńca-Kolasińska, and Bartłomiej Szafran
AGH University of Science and Technology, Faculty of Physics and Applied Computer Science, al. Mickiewicza 30, 30-059 Kraków, Poland
(Received 15 June 2017; revised manuscript received 16 November 2017; published 18 December 2017)

We consider a dilute fluorinated graphene nanoribbon as a spin-active element. The fluorine adatoms introduce a local spin-orbit Rashba interaction that induces spin precession for electron passing by. The spin precession involving a single adatom is infinitesimal and accumulation of the spin-precession events with many electron passages under adatoms is necessary to accomplish a spin flip. In order to arrange for this accumulation, a circular n-p junction can be introduced to the ribbon by, e.g., potential of the tip of an atomic force microscope. Alternatively, a fluorinated quantum ring can be attached to the ribbon. We demonstrate that the spin-flip probability can be increased in this manner by as much as three orders of magnitude. The Zeeman interaction introduces spin dependence of the Fermi wave vectors which changes the electron paths within the disordered system depending on the spin orientation. The effect destroys the accumulation of the spin-precession events in the n-p junction. For side-attached quantum rings, however, for which the electron path is determined by the confinement within the channel, the accumulation of the spin precession is robust against the Zeeman spin splitting.

DOI: 10.1103/PhysRevB.96.245307

I. INTRODUCTION

The coherent spin transport in semiconducting materials [1] is under extensive studies since the idea for the spin transistor was introduced [2]. Graphene [3] due to the absence of hyperfine interactions and long spin coherence times [4,5] is a good candidate for a spin conductor. However, pristine graphene is a poor material for spin-active elements due to the weakness of the spin-orbit interaction [6,7]. Enhancement of the spin-orbit coupling was proposed by deposition of graphene on transition-metal dichalcogenides (TMDC) [8,9]. The coupling with the TMDC layer gives rise to a strong Rashba interaction [9] that results from redistribution of the electron charge density and an appearance of the electric field component perpendicular to the graphene plane. Alternatively, the spin-orbit interaction can be introduced by adatoms [10], hydrogen [11–17], or fluorine [18–24]. The latter is 10 times more efficient than the former as the source of the spin-orbit coupling [22].

In this paper, we consider transport across the graphene nanoribbon [25] with a dilute fluorinated segment as a spin inverter of the Fermi level electrons that could be implemented as a spin transistor channel [2]. The procedure to detect the spin flips on the electron motion within the spin-orbit-coupled medium was recently demonstrated [26]. The system [26] employs two quantum point contacts which are transparent to a single spin direction only. The rotation of the electron spin on the way from one contact to the other results in the conductance drop.

We study the effects of the spin precession induced by the Rashba interaction near the adatoms. We find that in the absence of the external magnetic field, the spin-flip probability is very low, which we attribute to cancellation of the spin-precession effects by multiple electron backscattering since the direction of the spin precession in the Rashba field depends on the orientation of the electron momentum [2].

In order to strengthen the spin-orbit coupling effects, we introduce an n-p junction in an external magnetic field. The n-p junctions in graphene can be induced by electrostatic potential which moves the Dirac point above or below the Fermi level [3]. In the quantum Hall conditions, these junctions form waveguides that confine currents [27–34]. The confinement in the classical terms can be understood as a result of the Lorentz force pushing the electrons to the n-p junction at both its sides. The opposite orientation of the Lorentz force for the carriers of the conduction and valence bands in classical terms produces snake orbits [32–40] winding along the junction. The magnetic confinement of the current along the junction is supported for a single direction of the current only. The effects of the spin precession by the local Rashba interaction can be accumulated provided that the Fermi level electron passes many times under adatoms with weak backscattering. In order to recycle the electron passages, we consider a circular n-p junction defined by, e.g., an external gate of the scanning probe microscope [41–45]. In the quantum Hall conditions, the current comes to the junction from the edge and the lifetime of the localized resonances with the current circulation around the ring can be controlled by the gate potential, the Fermi energy [44], and the external magnetic field [45]. We find that for the current circulating around the junction, the spin-flip probability on the electron transfer can be increased by as much as three orders of magnitude.

We also consider the fluorinated ribbon in the quantum Hall conditions with the external potential removed. In strong magnetic fields, the localized resonances are associated with the current circulation from one adatom to the other and no backscattering along the path of incidence is possible. In these conditions, for a number of magnetic field values the spin-flip probability produces high peaks. For low magnetic field, we find a dip of conductance which is a signature of the weak localization effects that in graphene are present when the intervalley scattering is strong [46]. In the present problem, the adatoms as atomic scale perturbations to the lattice introduce strong intervalley scattering centers.

The effects of the accumulation of multiple spin flips require that the electron trajectory remains unaffected by the spin orientation. The dependence of the trajectory within

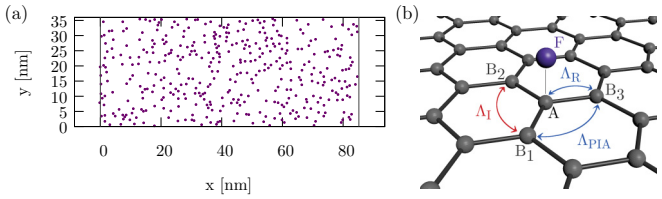

FIG. 1. (a) The considered graphene nanoribbon with 292 atoms across and the fluorinated segment. About 400 F adatoms are deposited at random (dots) within a part of nanoribbon that is 85.2 nm long. For the scattering problem, the electron is incident from the left. The pristine graphene ends of the ribbon are treated as the leads feeding and draining the charge and spin current from the system. (b) The fluorine adatom and its surroundings. The symbols refer to the local spin-orbit coupling Hamiltonian introduced with the adatom $H_{\rm SO}$ [see Eq. (4)].

the disordered system on the spin orientation appears via the Zeeman interaction and the resulting spin dependence of the Fermi wave vector. In order to preserve large spin-flip probability, the electron path across the fluorinated area needs to be weakly dependent on the wave vector. We show that this can be achieved with a fluorinated quantum ring side attached to the ribbon. For one of the perpendicular magnetic field orientations, the Fermi level wave function is injected to the ring provided that the Fermi energy is in resonance with states circulating within the ring [45]. The resulting spin precession is stable against the spin Zeeman interaction. Quantum rings are defined in graphene ribbons by well-established etching techniques [47–51] and the role of the magnetic focusing has been discussed recently [45,51].

II. THEORY

A. Hamiltonian

We use the atomistic π-band tight-binding Hamiltonian, which in the absence of the fluorine adatoms takes the form

$$H_0 = \sum_{\langle i,j\rangle}\sum_{\sigma}(t_{ij}c^{\dagger}_{i,\sigma}c_{j,\sigma} + \text{H.c.}), \tag{1}$$

where $c^{\dagger}_{i,\sigma}$ and $c_{i,\sigma}$ are the creation and annihilation operators for the electron on ith ion with spin σ. In this paper, we use the eigenstates of the z component of the spin $S_z = \frac{\hbar}{2}\sigma_z$ as the basis, so that the summation over spins runs over the eigenstates of the σ_z operator. The summation $\langle i,j\rangle$ runs over the nearest-neighbor carbon atoms and $t = -2.7$ eV is the hopping parameter.

We consider a nanoribbon which in the absence of the adatoms is a strip of a crystal lattice of a finite width [see Fig. 1(a)]. The experiments on graphene ribbons indicate a presence of the transport gap [52–54] near the charge neutrality point within which the system does not conduct electrical current. For that reason, we consider here a semiconducting armchair ribbon. For the proof of principle in Sec. III A, we take a ribbon that contains only three carbon atoms on its width. The rest of the results are obtained either for a thinner ribbon with 292 atoms across the width of $\simeq 35$ nm (Secs. III B, III C, III D, and III F) or for a wider ribbon (Sec. III E) with 1017 atoms across the width of $\simeq$125 nm. For the thinner (wider) ribbon the scattering region considered in this work is a central finite region 85.2 nm (127 nm) long with fluorine 400 (2165) adatoms in a dilute concentration. We also consider spin rotation within a fluorinated quantum ring of a circumference 283 nm (Sec. III F).

The locations of the fluorine atoms are generated at random with a uniform distribution. The results presented below are typical and quantitatively independent of the specific distribution. The position of the conductance peaks changes from one distribution to the other but the discussed physics does not. The fluorine atoms once adsorbed by graphene can only diffuse on its surface provided that the thermal excitations overcome migration barrier which for the fluorine adatoms is equal to 0.29 eV [55]. Therefore, the motion of the fluorine adatoms on the surface is frozen at low temperatures. The value changes with the carrier density level [56], but below we consider mainly conditions of the lowest subband transport, i.e., low Fermi energies near the charge neutrality point.

A fluorine adatom [see Fig. 1(b)] introduces additional terms to the Hamiltonian [22]

$$H' = H_0 + H_{\rm F} + H_{\rm SO}, \tag{2}$$

where $H_{\rm F}$ stands for the orbital, and $H_{\rm SO}$ the spin-orbit coupling effects. The orbital contribution $H_{\rm F}$ covers the level localized at the fluorine adatom (F) with the energy level $\varepsilon_f = -2.2$ eV and the hopping element $T = 5.5$ eV between the fluorine and the carbon atom (A) that form a vertical dimer [F-A, see Fig. 1(b)]:

$$H_{\rm F} = \varepsilon_f \sum_{\sigma}\hat{F}^{\dagger}_{\sigma}\hat{F}_{\sigma} + T\sum_{\sigma}(\hat{F}^{\dagger}_{\sigma}\hat{A}_{\sigma} + \hat{A}^{\dagger}_{\sigma}\hat{F}_{\sigma}), \tag{3}$$

where $\hat{F}_{\sigma}$ is the annihilation operator for electron in the fluorine ion with spin σ, and A_{σ} is the annihilation operator for the fluorinated carbon atom.

The three nearest-neighbor atoms of the fluorinated carbon A are denoted by B (see Fig. 1). The creation operator for the electron in the B atoms is $\hat{B}^{\dagger}_{i,\sigma}$. With this notation, the spin-orbital part has the form [22]

$$\begin{aligned} H_{\rm SO} = {} & \frac{i\Lambda^B_{\rm I}}{3\sqrt{3}}\sum_{\langle\langle i,j\rangle\rangle}\sum_{\sigma}\hat{B}^{\dagger}_{i,\sigma}\nu_{ij}(\hat{\mathbf{s}}_z)_{\sigma\sigma}\hat{B}_{j,\sigma} \\ & + \frac{2i\Lambda_{\rm R}}{3}\sum_{B_j\in C_{nn}}\sum_{\sigma\neq\sigma'}[\hat{A}^{\dagger}_{\sigma}(\hat{\mathbf{s}}\times\mathbf{d}_{{\rm A}j})_{z,\sigma\sigma'}\hat{B}_{j,\sigma'} + \text{H.c.}] \\ & + \frac{2i\Lambda^B_{\rm PIA}}{3}\sum_{\langle\langle i,j\rangle\rangle}\sum_{\sigma\neq\sigma'}\hat{B}^{\dagger}_{i,\sigma}(\hat{\mathbf{s}}\times\mathbf{d}_{ji})_{z,\sigma\sigma'}\hat{B}_{j,\sigma'}. \end{aligned} \tag{4}$$

The first sum is the intrinsic spin-orbit coupling in the Kane-Mele form [57] which is spin diagonal. The second term describes the Rashba interaction induced by the perpendicular electric field due to the deformation of the electron density by the adatom. The last term is the pseudospin-inversion-asymmetry next-nearest-neighbor term that results from deformation of the graphene lattice by the adatom [58]. The summation $\langle\langle i,j\rangle\rangle$ runs over the nearest neighbors of the fluorinated atom $\{B_1,B_2,B_3\}$. The coefficient ν_{ij} is $+1$ (-1) when the path from j to i via a common nearest neighbor k, $j\to k\to i$, is counterclockwise (clockwise) and $\mathbf{d}_{ij}$ is the unit vector in the xy plane oriented from ion j to i. The applied

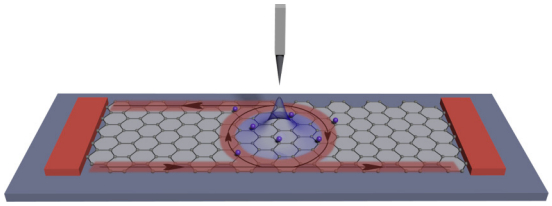

FIG. 2. The nanoribbon with F adatoms, and the n-p junction introduced by a tip of an atomic force microscope. The p region is induced below the tip. The arrows show the orientation of the edge and junction currents for the magnetic field oriented from above to the graphene plane.

spin-orbit coupling parameters [22] for 0.5% concentration of the fluorine atoms are $\Lambda_1^B = 3.3$ meV, $\Lambda_R = 11.2$ meV, and $\Lambda_{PIA}^B = 7.3$ meV. Both the Rashba and the pseudo inversion asymmetry (PIA) terms induce spin variation in the electron motion across the fluorinated area. However, for the applied parameters, the effect of the PIA is by an order of magnitude lower in terms of the spin-flipping transfer rate.

The orbital effects of the perpendicular external magnetic field are introduced to the Hamiltonian by modification of the hopping parameters. For the Hamiltonian of Eq. (2) put in a general form

$$H' = \sum_{k,l,\sigma,\sigma'} h_{k\sigma l\sigma'} c^\dagger_{k\sigma} c_{l\sigma'}, \tag{5}$$

in presence of the external magnetic field the hopping parameters are modified by the Peierls phase

$$H'_B = \sum_{k,l,\sigma,\sigma'} h_{k\sigma l\sigma'} \exp\left[\frac{2\pi i}{\Phi_0}\int_{\mathbf{r}_i}^{\mathbf{r}_j} \mathbf{A}\cdot\mathbf{dl}\right] c^\dagger_{k\sigma} c_{l\sigma'}, \tag{6}$$

where $\mathbf{A}$ is the vector potential, $\Phi_0 = h/e$ is the magnetic flux quantum, and $\mathbf{r}_i$ is the position of ith ion.

The interaction of the spin with the magnetic field oriented along the direction perpendicular to the graphene plane is introduced by the Zeeman interaction

$$H'_{B,Z} = H'_B + \frac{1}{2} g\mu_B B \sum_{k,\sigma} (\hat{\mathbf{s}}_z)_{\sigma\sigma} c^\dagger_{k\sigma} c_{l\sigma}, \tag{7}$$

with μ_B the Bohr magneton and $g = 2$.

B. Quantum rings: Induced at the n-p junction and side attached

In order to form an n-p junction within the ribbon, we introduce an external potential of, e.g., a charged tip of an atomic force microscope [44,45,59] (see Fig. 2). The original tip potential is of the Coulomb form which is screened by deformation of the electron gas within the conducting plane. The Schrödinger-Poisson equations for the tip screened by the two-dimensional electron gas produce an effective tip potential [59] which is close to the Lorentz form

$$W(x,y) = \frac{V_t}{1 + [(x-x_t)^2 + (y-y_t)^2]/d^2}, \tag{8}$$

where x_t, y_t is the tip position over the plane, and d is the effective width of the tip potential that is of the order of the tip-electron gas distance [59], and V_t depends on the charge accumulated by the tip. We adopt $V_t = 400$ meV and $d = 4.92$ nm as in the previous paper [44]. In Hamiltonian H_0 given by Eq. (1), $W_i = W(x_i, y_i)$. For the work point we set $E_F = 60$ meV with the fluorine concentration $\eta = 0.5\%$ unless stated otherwise.

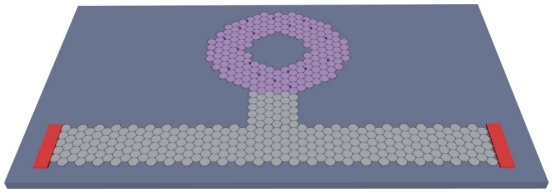

FIG. 3. Schematics of a fluorinated quantum ring side attached to the graphene ribbon.

In presence of the Zeeman effect, large spin flips can be obtained when the electron path remains the same for both spin orientations. We arrange for these conditions with a quantum ring side attached to the ribbon (see Fig. 3). The ribbon that is 293 atoms wide is considered for this purpose. The external and internal radii of the ring are 27 and 63 nm, respectively, and the arm of the ring contains about 293 atoms along its radius. The fluorine is adsorbed only within the ring.

C. Evaluation of spin-resolved conductance

The implementation of the Landauer approach in this work is based on a direct solution of the Schrödinger equation $H\Psi = E_F\Psi$ with the boundary conditions proper for the scattering problem of the Fermi level electrons incident from the left lead (see Fig. 4). We first explain how the asymptotic states in the leads made of the graphene ribbon are calculated, next explain the version of the wave-function-matching technique [60] applied in this work, and then explain how the spin-resolved contributions to conductance are calculated.

1. Eigenstates of the leads

Boundary conditions in the wave-function-matching (WFM) method [60] relate the scattering wave function to the eigenstates of the lead. Here, we explain how the latter are determined. Let us consider an infinite chain of identical elementary cells numbered by u as an extension of the input lead (see Fig. 5) to $u = -\infty$.

The Hamiltonian matrix for the infinite ribbon that serves as the input lead can be put in the form

$$\mathcal{H} = \begin{pmatrix} \ddots & \cdots & 0 & 0 & \\ \vdots & \mathbf{H}_{u-1} & \mathbf{B}^\dagger_{u-1} & 0 & 0 \\ 0 & \mathbf{B}_{u-1} & \mathbf{H}_u & \mathbf{B}^\dagger_u & 0 \\ 0 & 0 & \mathbf{B}_u & \mathbf{H}_{u+1} & \vdots \\ & 0 & 0 & \cdots & \ddots \end{pmatrix}, \tag{9}$$

where matrix $\mathbf{H}_u$ is the Hamiltonian of a single elementary cell u. No adatoms are contained within the leads, so that the elements of the Hamiltonian are determined by hopping between the nearest neighbors as in the Hamiltonian (1).

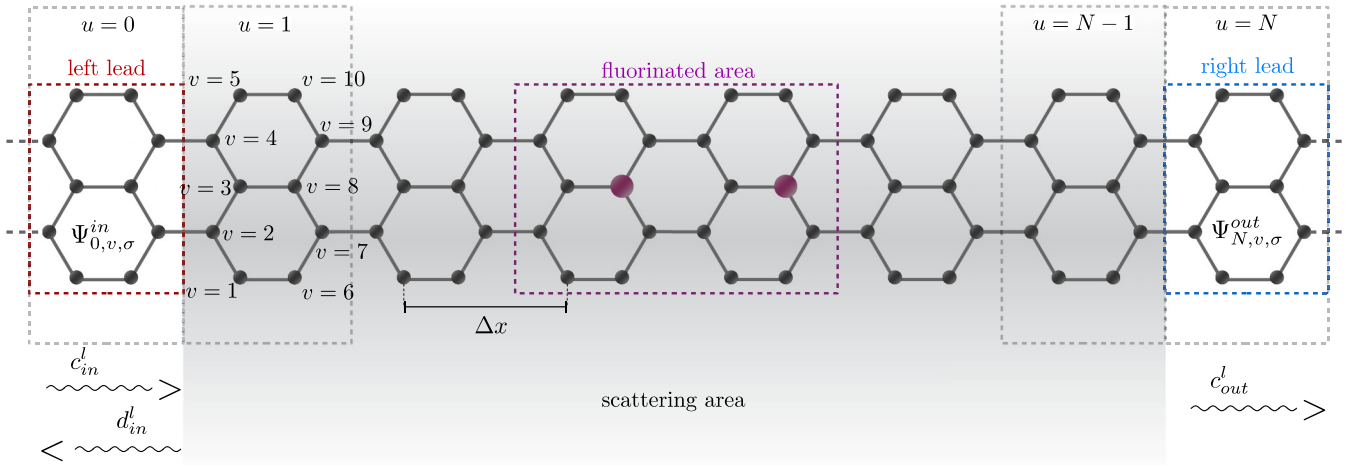

FIG. 4. Schematics of the computational box with the fluorinated scattering area and the elementary cells where the asymptotic wave functions of the ribbons are matched to the scattering wave function for integration of the scattering problem. The electron is incident from the left with the amplitude c_{in}. c_{out} stands for the amplitude of the wave function transferred to the output lead and d_{in} for the wave functions backscattered to the input lead. u numbers the elementary cells and v the nodes in the elementary cells.

The matrix $\mathbf{B}_u$ stands for the hopping between cells u and $u+1$. Matrices $\mathbf{H}_u$ and $\mathbf{B}_u$ are the size of $2n \times 2n$ where n is the number of atoms inside the elementary cell and factor 2 arises from the spin degree of freedom. For an ideal periodic infinite ribbon, matrices $\mathbf{H}_u$ and $\mathbf{B}_u$ are identical, therefore, the u symbol will be omitted from this point. The eigenfunction of the Hamiltonian $\mathcal{H}$ can be divided on eigenfunctions for each elementary cell

$$\boldsymbol{\psi} = \begin{pmatrix} \vdots \\ \psi_{u-1} \\ \psi_u \\ \psi_{u+1} \\ \vdots \end{pmatrix}, \tag{10}$$

where ψ_u is the vector of size $2n$. The Hamiltonian eigenfunction satisfies the equation

$$-\mathbf{B}\psi_{u-1} + (E\mathbf{I} - \mathbf{H})\psi_u - \mathbf{B}^\dagger\psi_{u+1} = 0. \tag{11}$$

The solutions in ideal lead modes have a Bloch form

$$\psi_u = \psi_{u-1}e^{ik\Delta x}, \tag{12}$$

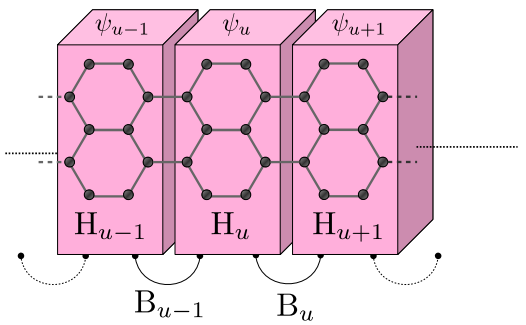

FIG. 5. The WFM implementation diagram. System is divided into elementary cells u with eigenfunctions ψ_u describing all orbitals inside cell. The matrix $\mathbf{H}_u$ is the Hamiltonian of a single elementary cell u and $\mathbf{B}_u$ stands for the hopping between cells u and $u+1$.

where Δx is the length of an elementary cell of the lead. Using the form (12) of the wave function in substitution

$$\psi_{u-1} = \chi, \quad \psi_u = \lambda\chi, \quad \psi_{u+1} = \lambda^2\chi,$$

where $\lambda = \exp(ik\Delta x)$, we get

$$-\mathbf{B}\chi + \lambda(E\mathbf{I} - \mathbf{H})\chi - \lambda^2\mathbf{B}^\dagger\chi = 0, \tag{13}$$

For $\eta = \lambda\chi$, Eq. (13) above can be written as

$$\left[\begin{pmatrix} 0 & \mathbf{I} \\ -\mathbf{B} & E\mathbf{I} - \mathbf{H} \end{pmatrix} - \lambda\begin{pmatrix} \mathbf{I} & 0 \\ 0 & \mathbf{B}^\dagger \end{pmatrix}\right]\begin{bmatrix} \chi \\ \eta \end{bmatrix} = 0. \tag{14}$$

The above eigenproblem has $4n$ solutions: $2n$ left-going and $2n$ right-going modes, evanescent or propagating. The mth eigenvalue satisfies $|\lambda_{m,\sigma}| < 1$ ($|\lambda_{m,\sigma}| > 1$) for the evanescent modes decaying to the right (left). For the propagating modes of Bloch waves, the eigenvalue satisfies $\lambda_{m,\sigma} = \exp(ik_m\Delta x)$, with real k_m, hence, $|\lambda_{m,\sigma}| = 1$. The eigenstates for the mth subband with the wave vector k_m and spin σ at the node v in the uth elementary cell of the lead can be written as

$$\psi^{k_m}_{u,v,\sigma} = \chi^{k_m}_{v,\sigma}e^{ik_m u\Delta x}, \tag{15}$$

where $\chi^{k_m}_{v,\sigma}$ is transverse mode of wave vector k_m with spin σ at the v site.

The Hamiltonian eigenfunction in the input lead (see Fig. 4) in general is a superposition of the incident electron states with wave vectors k^+ and backscattered states with wave vectors k^-:

$$\Psi^{\text{in}}_{u,v,\sigma} = \sum_l \left(c^l_{\text{in}}\chi^{k^+_l}_{v,\sigma}e^{ik^+_l u\Delta x} + d^l_{\text{in}}\chi^{k^-_l}_{v,\sigma}e^{ik^-_l u\Delta x}\right), \tag{16}$$

where the summation over l runs over the subbands appearing at the Fermi level. At the output channel we have only the transferred, right-going waves

$$\Psi^{\text{out}}_{u,v,\sigma} = \sum_l c^l_{\text{out}}\chi^{k^+_l}_{v,\sigma}e^{ik^+_l u\Delta x}. \tag{17}$$

We solve for the scattering wave function Ψ that is an eigenstate of the Hamiltonian for an assumed Fermi energy

that is glued to the boundary conditions given by Eqs. (16) and (17) for each incoming subband separately setting $c^l_{\rm in} = \delta_{lm}$, for the electron incident from the subband m. The solution of the scattering problem and application of the wave-function matching is explained in the following subsection.

2. Wave-function matching

Let us denote by $\boldsymbol{H_S}$ the Hamiltonian matrix for the scattering region, which contains all the hoppings between the spin orbitals within the computational box. By vector $\boldsymbol{\Psi_S}$ we denote the spin-orbital wave functions at each ion in the computational box (see Fig. 4). The Fermi level scattering problem can be put in form of a linear system of equations

$$\left\{\boldsymbol{H_S} + \begin{pmatrix} \boldsymbol{H_L} & 0 & 0 \\ 0 & 0 & 0 \\ 0 & 0 & \boldsymbol{H_R} \end{pmatrix} - \boldsymbol{I}\,E_F\right\}\begin{pmatrix} \boldsymbol{\Psi_L} \\ \boldsymbol{\Psi_S} \\ \boldsymbol{\Psi_R} \end{pmatrix} = \begin{pmatrix} \boldsymbol{\xi} \\ 0 \\ 0 \end{pmatrix}, \quad (18)$$

where $\boldsymbol{\xi}$ is the self-energy of the left lead, $\boldsymbol{\Psi}_L$ and $\boldsymbol{\Psi}_R$ stand for the wave function in the 0th and Nth elementary cells (see Fig. 4), $\boldsymbol{H_L}$ and $\boldsymbol{H_R}$ describe the bonding of the wave function in the scattering area with the left and right leads. The form of the terms that results from the wave-function matching is given and explained below.

In the $u = 0$ elementary cell (see Fig. 4), the scattering wave function in the left output lead takes the form

$$\Psi^{\rm in}_{0,v,\sigma} = c_{\rm in}\chi^{k^+_{\rm in}}_{v,\sigma} + \sum_l d^l_{\rm in}\chi^{k^-_l}_{v,\sigma}, \quad (19)$$

where the term with $c_{\rm in}$ describes the incident electron with wave vector $k^+_{\rm in}$ and the sum stands for the superposition of the backscattered electron waves. We project the wave function (16) on the eigenstates of the leads $\chi^{k_{l'}}$:

$$\langle\chi^{k^-_{l'}}_{v,\sigma}|\Psi^{\rm in}_{0,v,\sigma}\rangle = \sum_l c^l_{\rm in}\langle\chi^{k^-_{l'}}|\chi^{k^+_l}\rangle + \sum_l d^l_{\rm in}\langle\chi^{k^-_{l'}}|\chi^{k^-_l}\rangle, \quad (20)$$

where $\langle A|B\rangle = \sum_i A^*_i B_i$ denotes the scalar product within a single elementary cell. Defining matrices $\mathbf{B}_{l',l} = \langle\chi^{k^-_{l'}}|\chi^{k^+_l}\rangle$, $\mathbf{S}_{l',l} = \langle\chi^{k^-_{l'}}|\chi^{k^-_l}\rangle$, and the vector $\mathbf{A}_{l'} = \langle\chi^{k^-_{l'}}|\Psi^{\rm in}_0\rangle$, we can rewrite Eq. (20) in a matrix form

$$\mathbf{A} = \mathbf{B}\mathbf{c}_{\rm in} + \mathbf{S}\mathbf{d}_{\rm in}, \quad (21)$$

from which we evaluate the backscattered amplitudes

$$d^l_{\rm in} = \sum_{l'}(\mathbf{S}^{-1})_{l,l'}\mathbf{A}_{l'} - \sum_{l',j}(\mathbf{S}^{-1})_{l,j}\mathbf{B}_{j,l'}\mathbf{c}^{l'}_{\rm in}. \quad (22)$$

In order to plug the result into the scattering problem, we calculate the derivative of the wave function

$$\begin{aligned}\frac{1}{\Delta x}\left(\Psi^{\rm in}_{0,v,\sigma} - \Psi^{\rm in}_{-1,v,\sigma}\right) &= c_{\rm in}\chi^{k^+_{\rm in}}_{v,\sigma}\frac{1}{\Delta x}(1 - e^{-ik^+_{\rm in}\Delta x}) \\ &+ \sum_l d^l_{\rm in}\chi^{k^-_l}_{v,\sigma}\frac{1}{\Delta x}(1 - e^{-ik^-_l\Delta x}), \end{aligned} \quad (23)$$

from where we get the equation for the wave function in the first elementary cell of the input lead outside the computational box

$$\Psi^{\rm in}_{-1,v,\sigma} = \Psi^{\rm in}_{0,v,\sigma} - c_{\rm in}\chi^{k^+_{\rm in}}_{v,\sigma}\Delta_{k^+_{\rm in}} - \sum_l d^l_{\rm in}\chi^{k^-_l}_{v,\sigma}\Delta_{k^-_l} \quad (24)$$

or, explicitly,

$$\begin{aligned}\Psi^{\rm in}_{-1,v,\sigma} = \chi^{k^+_{\rm in}}_{v,\sigma}e^{-ik^+_{\rm in}\Delta x} + \sum_{l,l'}(\mathbf{S}^{-1})_{l,l'} \\ \times\left[\sum_{v'}\left(\chi^{k^-_{l'}}_{v',\sigma}\right)^*\Psi_{0,v',\sigma} - \mathbf{B}_{l',in}\right]\chi^{k^-_l}_{v,\sigma}e^{-ik^-_l\Delta x}.\end{aligned} \quad (25)$$

The above expression is plugged into the scattering eigenequation when the hopping between the $u = 0$ and -1 elementary cell appears (see Fig. 4). The bonding introduces the following correction to the scattering Hamiltonian:

$$\boldsymbol{H_L}\boldsymbol{\Psi_L} = t\sum_{l,l'}(\mathbf{S}^{-1})_{l,l'}\sum_{v'}\left(\chi^{k^-_{l'}}_{v',\sigma}\right)^*\Psi_{0,v',\sigma}\chi^{k^-_l}_{v,\sigma}e^{-ik^-_l\Delta x}. \quad (26)$$

The components of the sum (25) that are independent of Ψ_0 with the hopping to the $u = -1$ cell produce the self-energy correction of the form

$$\boldsymbol{\xi} = -t\left(\chi^{k^+_{\rm in}}_{v,\sigma}e^{-ik^+_{\rm in}\Delta x} + \sum_{l,l'}(\mathbf{S}^{-1})_{l,l'}\mathbf{B}_{l',in}\chi^{k^-_l}_{v,\sigma}e^{-ik^-_l\Delta x}\right). \quad (27)$$

For the last cell in the computational box $u = N$, the wave function is

$$\Psi^{\rm out}_{N,v,\sigma} = \sum_l c_{\rm out}\chi^{k^+_l}_{v,\sigma}e^{iNk^+_l\Delta x}. \quad (28)$$

The projection on the lead eigenstates produces

$$\begin{aligned}\langle\chi^{k^+_{l'}}_{v,\sigma}e^{iNk^+_{l'}\Delta x}|\Psi^{\rm out}_{N,v,\sigma}\rangle &= \sum_l c^l_{\rm out}\langle\chi^{k^+_{l'}}e^{iNk^+_{l'}\Delta x}|\chi^{k^+_l}e^{iNk^+_l\Delta x}\rangle \\ &= \sum_l \mathbf{S}'_{l',l}c^l_{\rm out}\end{aligned} \quad (29)$$

and

$$c^l_{\rm out} = (\mathbf{S}')^{-1}_{l',l}\langle\chi^{k^+_{l'}}_{v,\sigma}e^{iNk^+_{l'}\Delta x}|\Psi^{\rm out}_{N,v,\sigma}\rangle. \quad (30)$$

Using the similar procedure as above, we calculate the derivative of the wave function between the last elementary cell $u = N$ and the first one outside the computational box $u = N + 1$. We obtain

$$\begin{aligned}\frac{1}{\Delta x}\left(\Psi^{\rm out}_{N+1,v,\sigma} - \Psi^{\rm out}_{N,v,\sigma}\right) &= \sum_l c^l_{\rm out}\chi^{k^+_l}_{v,\sigma}\frac{1}{\Delta x}e^{iNk^+_l\Delta x}(e^{ik^+_l\Delta x} - 1) \\ &= \sum_l c^l_{\rm out}\chi^{k^+_l}_{v,\sigma}\frac{1}{\Delta x}e^{iNk^+_l\Delta x}\Delta_{k^+_l}, \end{aligned} \quad (31)$$

from which we get the wave function outside the right side of the computational box

$$\Psi^{\rm out}_{N+1,v,\sigma} = \Psi^{\rm out}_{N,v,\sigma} + \sum_l c^l_{\rm out}\chi^{k^+_l}_{v,\sigma}e^{iNk^+_l\Delta x}\Delta_{k^+_l}. \quad (32)$$

With the expression for $c^l_{\rm out}$ given by Eq. (30), we obtain an explicit form

$$\Psi^{\rm in}_{N+1,v,\sigma} = \sum_{l,l'} (\mathbf{S}^{-1})_{l,l'} \sum_{v'} \left(\chi^{k^+_{l'}}_{v',\sigma}\right)^* \Psi_{N,v',\sigma} \chi^{k^+_l}_{v,\sigma} e^{ik^+_l \Delta x}. \quad (33)$$

The hopping between the N and $N+1$ elementary cells produces the correction to the Hamiltonian in the form

$$\boldsymbol{H_R \Psi_R} = t \sum_{l,l'} (\mathbf{S}^{-1})_{l,l'} \sum_{v'} \left(\chi^{k^+_{l'}}_{v',\sigma}\right)^* \Psi_{N,v',\sigma} \chi^{k^+_l}_{v,\sigma} e^{ik^+_l \Delta x}. \quad (34)$$

No self-energy vector appears here since Eq. (33) does not contain terms independent of the wave function Ψ_N.

3. Spin-resolved conductance

Once the quantum scattering problem is solved we may proceed to evaluation of conductance. For the Hamiltonian in form (6), the current flowing along the π bonds between m and m' ions is calculated as

$$J_{m\sigma m'\sigma'} = \frac{i}{h} \sum_{\sigma,\sigma'} [h_{m\sigma m'\sigma'} \Psi^*_{m,\sigma} \Psi_{m',\sigma'} - h_{m'\sigma' m\sigma} \Psi^*_{m',\sigma'} \Psi_{m,\sigma}], \quad (35)$$

where $\Psi_{m,\sigma}$ is the σ spin component of the wave function at the mth ion. The formula (35) accounts for the transfer of the current from one component of the spin to the other provided that the Hamiltonian contains the spin-orbit coupling components. This is indeed the case near the adatoms. Outside the fluorinated area the spin currents are conserved and can be calculated from Eq. (35) for each spin component.

For each Hamiltonian eigenstate in the leads with wave vector k^+_m we calculate the current fluxes

$$\phi_{k^+_m} = \sum_{i,n_i,\sigma,\sigma'} J_{i\sigma n_i \sigma'}, \quad (36)$$

where i are the indices of the atoms across the ribbon and n_i are their left (right) nearest neighbors in the ribbon left (right) lead where the flux is calculated. The electron transfer probability from the subband n to the subband m is calculated as

$$T_{mn} = \left| \frac{c^m_{\rm out}}{c^n_{\rm in}} \right|^2 \left| \frac{\phi_{k^+_m}}{\phi_{k^+_n}} \right|, \quad (37)$$

where $c^m_{\rm out}$ and $c^n_{\rm in}$ are the scattering amplitudes of the transferred and incident wave functions, in the m and n modes, respectively. The overall conductance is calculated by summation over the subbands at the Fermi level

$$G = G_0 \sum_{mn} T_{mn} \quad (38)$$

with the flux quantum $G_0 = e^2/h$.

Since the spin-orbit coupling is absent in the leads, the subbands have well-defined z components of the spin $\hbar/2$ which we denote by u or $-\hbar/2$ which we denote by d. So, the set of indices $\{m\}$ of subbands can be separated into sets of spin-up and spin-down subbands $\{m\} = \{m_u\} + \{m_d\}$. Accordingly, the summation in the formula for conductance

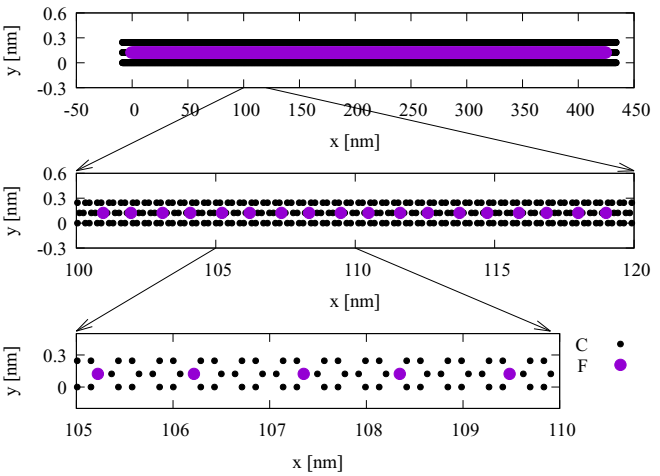

FIG. 6. A narrow ribbon that is considered in Sec. III A with the fluorine concentration $\eta \approx 6.7\%$. The position of the C and F ions are marked with black and purple dots, respectively.

can be divided into separate spin-resolved sums

$$\begin{aligned} G &= G_0 \sum_{m_u n_u} T_{m_u n_u} + G_0 \sum_{m_u n_d} T_{m_u n_d} \\ &\quad + G_0 \sum_{m_d n_u} T_{m_d n_u} + G_0 \sum_{m_d n_d} T_{m_d n_d} \\ &= G_{uu} + G_{ud} + G_{du} + G_{dd} \end{aligned} \quad (39)$$

with the spin-conserving contributions G_{uu}, G_{dd} and the spin-flipping ones G_{du}, G_{ud}.

III. RESULTS AND DISCUSSION

A. Accumulation of the spin-precession events ($B = 0$)

As a proof of principle for accumulation of the local spin-precession events, we consider a narrow ribbon depicted in Fig. 6. The ribbon is a sequence of hexagons with the fluorine atoms placed near the junctions of one hexagon to the other (Fig. 6). No external magnetic field is applied and the electron is injected to the system with spin-down orientation from the left-hand side. The positions of the F atoms are repeated periodically within the ribbon, so the G dependence on E_F forms a series of resonances as for a superlattice band filter [61]. We set the value of the Fermi energy $E_F = 4.620\,512$ eV marked by the dot in Fig. 7 for which the system is transparent for electrons and look at the average spin z and x components calculated for subsequent hexagonal elementary

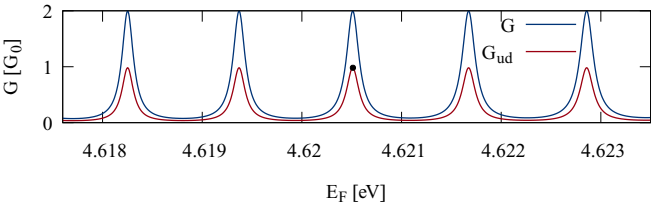

FIG. 7. The conductance G and its spin-flip contributions for the system given in Fig. 6. The narrow range of E_F was chosen to distinguish resonances.

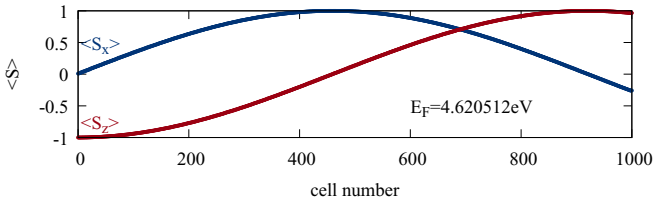

FIG. 8. The average x and z components of the spin calculated for subsequent elementary cells for $E_F = 4.620\,512$ eV (see the dot in Fig. 7) for which the system is transparent for the Fermi electron. The electron is incident from the left with $\mathbf{s}_z = -1$ orientation. The average y component (not shown) is nearly 0 all along the ribbon.

cells of the ribbon in Fig. 8. For the resonant energy electron on its way across the system comes to fluorinated carbon atom with the same momentum and no backscattering is present. In total, there are 400 F atoms along the ribbon with the concentration $\eta \approx 6.7\%$. The overall conductance G and the spin-flip contribution are depicted in Fig. 7.

Although an effect of a single fluorine atom to the orientation of the electron spin is very small, we can see that upon transition below 400 fluorine atoms is enough to rotate the electron spin from the $-z$ the $+z$ orientation. The source of the spin-flip transfer in the considered system is the Rashba component of the Hamiltonian that is due to the local electric field introduced by adatoms.

The Rashba spin-orbit interaction due to the adatom introduces an effective magnetic field $\mathbf{B}_{\mathrm{SO}} = C(\mathbf{p} \times \mathbf{E})$ [62], where C is a constant, $\mathbf{p}$ the electron momentum, and $\mathbf{E}$ the electric field vector. For the planar motion $p_z = 0$ and the vertical electric field $E_z \neq 0$ induced by the adatom, the $\mathbf{B}_{\mathrm{SO}}$ is oriented along the y direction, i.e., in plane and perpendicular to the momentum orientation. The spin of the electron moving within the graphene layer precesses around $\mathbf{B}_{\mathrm{SO}}$ [2,26,63]: in the case considered in Fig. 8 from the orientation to below the ribbon $(-z)$ through the orientation along the ribbon (x) for about 480th hexagonal cell of the ribbon to the orientation above the ribbon $(+z)$ for the 960th cell.

B. Transport across a fluorinated layer at $B = 0$

The results of the preceding subsection demonstrate that the spin flip is possible upon electron transition under many F adatoms. Nevertheless, an experimental fabrication of the extremely narrow ribbon with ordered F positions is rather unlikely. Let us then consider the ribbon which is 292 atoms wide with random locations of the F atoms [see Fig. 1(a)].

The calculated electron transfer probability as a function of the Fermi energy is given in Fig. 9(a). The blue line indicates the ribbon conductance in the absence of the fluorine atoms, which in G_0 units is equal to the number of subbands that carry the flux to the right. The adatoms perturb the system and induce strong backscattering, which induces the drop of conductance in Fig. 9(a) with introduction of the adatoms. In the scattering region, only 0.5% of the carbon atoms are fluorinated, but the perturbation of the potential by adatoms is strong and their random locations rule out the transparency of the system at resonances as in the ordered system of Fig. 7.

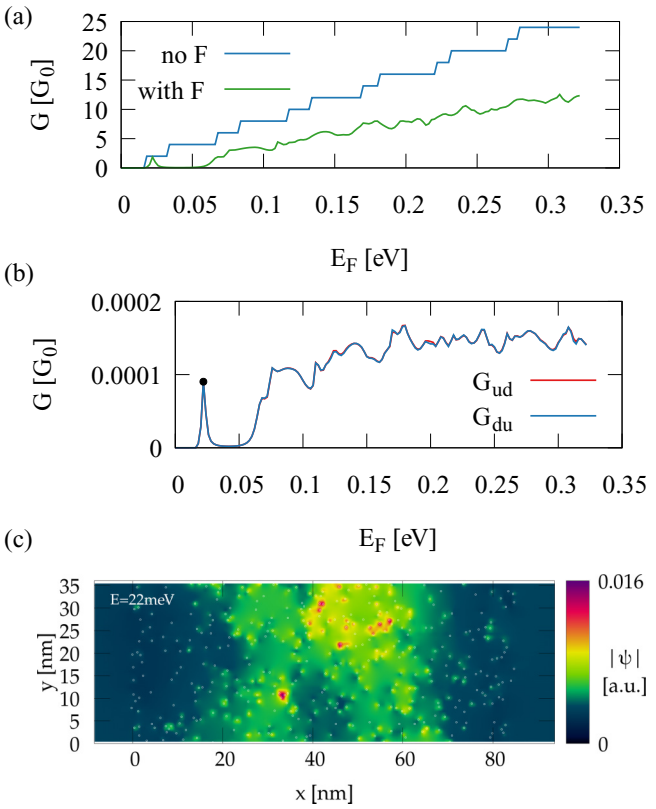

FIG. 9. (a) Conductance for a pristine semiconducting armchair nanoribbon (blue line) and the one with 400 fluorine adatoms (green line) as functions of the Fermi energy at $B = 0$. (b) The spin-flipping contribution to conductance: the probability of the spin inversion from one σ_z eigenstate to the other upon transition across the fluorinated segment. (c) The amplitude of the scattering wave function for the peak at $E = 0.022$ eV marked by the black dot in (b).

Only a very low spin-flip probability is observed [Fig. 9(b)]. A local maximum of the spin-flip probability near 0.022 eV [Fig. 9(b)] is associated with a quasibound resonance [Fig. 9(a)] that is supported by a group of adatoms [see the amplitude of the scattering wave function at Fig. 9(c)].

The electron backscattering by adatoms inverts the direction of the electron motion, and on the electron way back the spin precession [63] due to the local Rashba interaction is reversed [see $\Delta\varphi$ for the incident and $-\Delta\varphi$ for the backscattered motion in Fig. 10(a)], hence, the near cancellation of the overall spin-precession events that results in the low spin-flipping conductance contribution in Fig. 9(b).

Figure 9(b) shows that the spin-flipping effects of the electron passage across the fluorinated layer are very weak. Formation of a resonance supported by adatoms [Fig. 9(c)] with the Fermi electron experiencing a multiple scattering increases the electron dwelling time in the area where the spin-orbit coupling is present and enhances the spin-flip probability [see Fig. 9(b) near $E_F = 0.022$ eV], which however remains very low.

C. Recycling the electron passages: Circulation around n-p junction (Zeeman interaction neglected)

In order to accumulate the effects of the spin precession, we introduced a n-p junction to the system defined by a

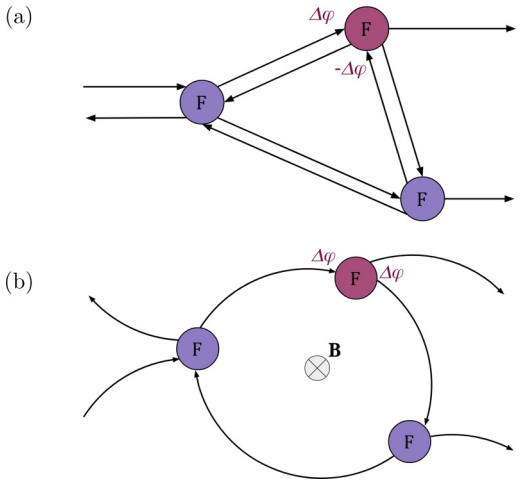

FIG. 10. Classical electron paths scattered by the fluorine adatoms. Electron is incident from the left. In the absence of the magnetic field (a) the electron gets backscattered and the spin-precession angle $\Delta\varphi$ due to the Rashba interaction induced by a single F adatom marked by red is reversed by the backscattering $-\Delta\varphi$. In the quantum Hall conditions (b) backscattering along the same path is absent due to the magnetic deflection of the trajectories. For closed paths, the precession angle accumulates at each electron transition near an adatom.

gate potential, a tip of an atomic force microscope (see Fig. 2). In the perpendicular magnetic field, it is possible to induce long-living resonances localized at the n-p junction introduced by an external gate [44]. Moreover, the electron backscattering along the same path as in Fig. 10(a) is no longer present in the quantum Hall conditions. The schematics of the current circulation in the quantum Hall conditions is given in Fig. 2. For the magnetic field oriented to the graphene plane $\mathbf{B} = (0,0,-|B|)$, the classical Lorentz force pushes the moving conduction band carriers to the right of their momentum. In consequence, the incident and transferred current of conduction band electrons flows along the lower edge, while the backscattering mediated by the circular n-p junction goes through the upper edge. For the considered magnetic field orientation the current circulation around the n-p junction is clockwise (see Fig. 2), and the currents are stabilized for this single current orientation only [45]. Formation of the waveguide at the n-p junction separated from the edge of the ribbon requires formation of the quantum Hall conditions. The separation of the edge and junction current occurs when a cyclotron radius fits between the edge and the junction. For the cyclotron orbit given by the magnetic length $l_B = \sqrt{\hbar/eB} = 26[\mathrm{nm}]/\sqrt{B[\mathrm{T}]}$, the ribbon width w and the diameter of the junction d, the condition reads as $2l_B < (w-d)/2$, which for the ribbon with 292 atoms considered here produces the condition $B > 12$ T.

In presence of the fluorine the conductance undergoes oscillations (Fig. 11) which are not as perfectly periodic as for the clean ribbon [44], nevertheless, an approximate periodicity at higher B can be noticed. The contribution to the conductance from the spin-flip transfer is, at higher magnetic field, large, reaching $0.2G_0$. Moreover, the spin flips, at higher B, become periodic and correlated with the conductance maxima

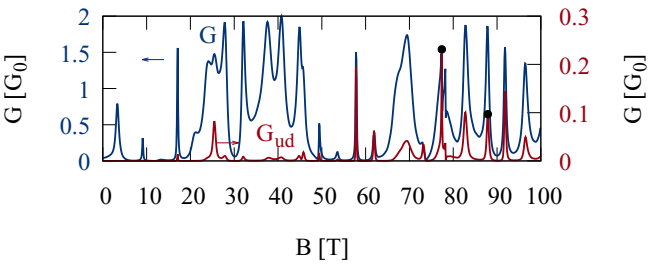

FIG. 11. The overall (left axis, blue line) conductance and its spin-flipping contribution (right axis, red line) for the fluorinated n-p juncion. Black dots represent peaks for which scattering densities are presented below.

(cf. Fig. 11). Note that the maximal spin-flip transfer probability is increased by as much as three orders of magnitude with respect to Fig. 9(b).

Figure 12 shows the scattering charge density at the carbon atoms for 77.4 and 87.9 T, for which the spin-flipping contribution to conductance presents local maxima (Fig. 11). Figure 12(b) presents a typical scattering density distribution for the resonances encircling the n-p junction perturbed by the adatoms. In Fig. 12(a), a localization of the resonance at an adatom in the central, p conductivity, region can be seen. The resonances localized inside potential barrier were discussed in Ref. [44]. Their long lifetime results from the direction of current circulation [44] that the Lorentz force shifts to the center of the barrier and keeps the scattering density off the n-p junction.

Note that the peaks of the overall conductance [Fig. 11(a)] and its spin-flipping contribution [Fig. 11(b)] are correlated already for $B \geqslant 10$ T and the spin-flipping peaks increase in amplitude for higher B. This results from an increasing magnetic confinement of the currents near the edge and the junction which decreases the coupling between the edge currents and the circular junction currents (Fig. 2) [44,45]. The effect results in reduction of the coupling of the n-p junction to the edge. The lifetime of the resonances is increased along

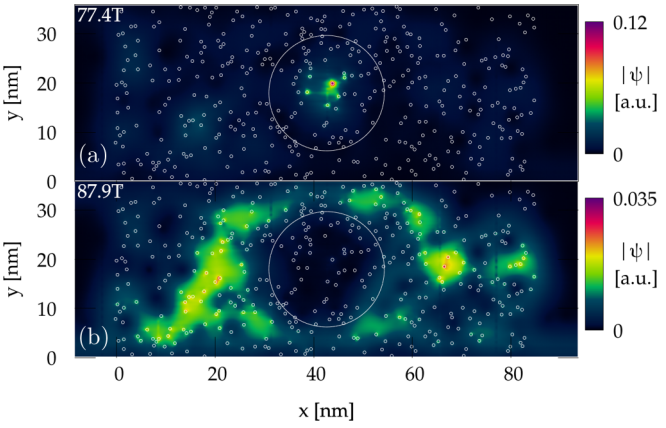

FIG. 12. The amplitude of the scattering wave function for two peaks of conductance of Fig. 11 (black dots) at 77.4 T (a) and 87.9 T (b). The circle indicates the position of the n-p junction defined by $E_F = V(x,y)$. The fluorine adatoms are marked with tiny white circles.

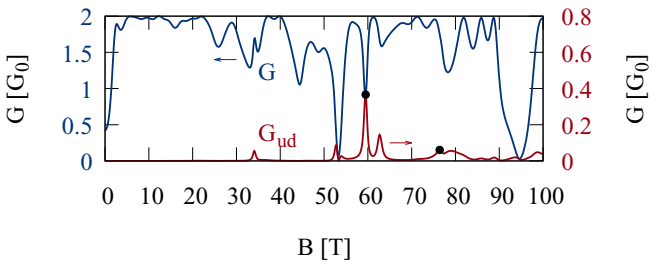

FIG. 13. Same as Fig. 11 only without the external potential defining the n-p junction.

with the effects of the accumulation of the spin-precession phase shifts.

D. Resonances in the disordered sample (Zeeman interaction neglected)

The conductance with the external potential of the precedent section removed is plotted in Fig. 13. We observe an aperiodic dependence of conductance as a function of the external magnetic field. A conductance dip at $B = 0$ [Fig. 14(a)] is characteristic to the weak localization as for

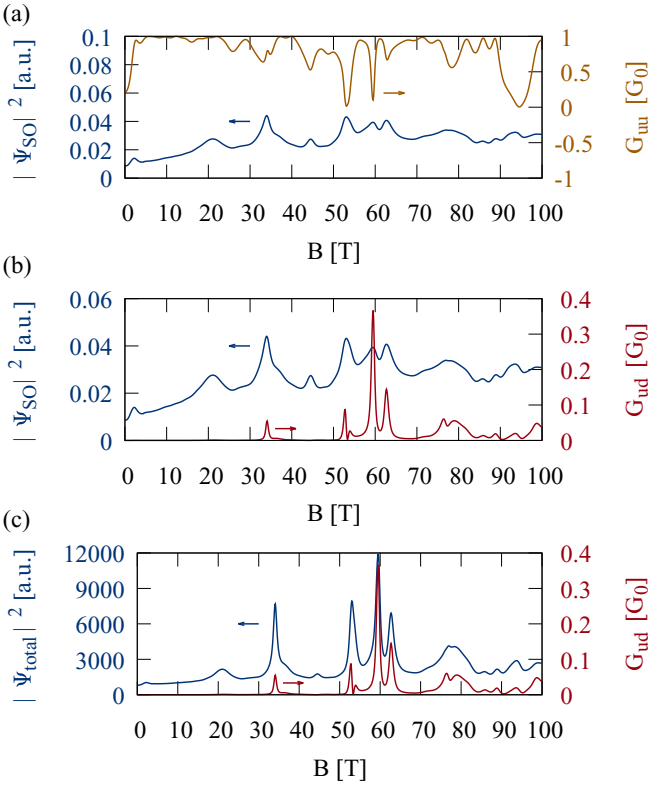

FIG. 14. (a) The spin-conserving component of conductance (orange line, right axis) and the fraction of the scattering density localized in the area where the spin-orbit coupling interaction is present (blue line, left axis). (b) Same as (a), only the red line indicates the spin-flipping contribution to conductance. (c) Same as (b), only with the blue line that indicates the integral of the scattering density within the entire fluorinated ribbon segment for the normalized electron incidence amplitude.

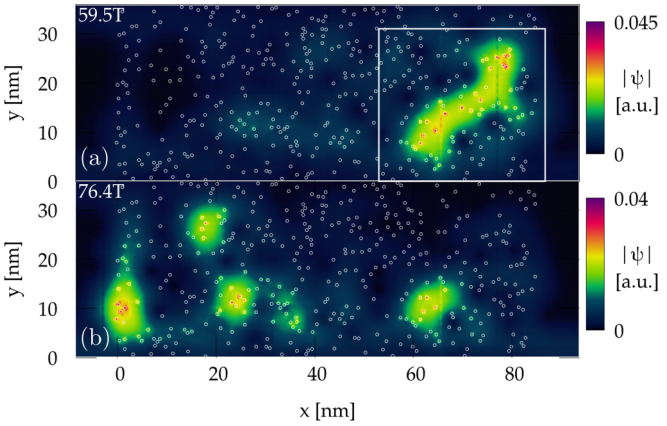

FIG. 15. The amplitude of the scattering wave function for two peaks of conductance of Fig. 13 (black dots) at 59.5 T (a) and 76.4 T (b). The fluorine adatoms are marked with tiny white circles.

a disordered conductor. In graphene, the weak localization dip is observed when the intervalley scattering is strong [46]. In this paper, the role of the atomic scale defects that induce the intervalley scattering is played by the adatoms themselves. The intervalley scattering length can be estimated by the average distance between the F atoms which is $\simeq$1.5 nm for the dilute 0.5% F concentration. In this paper, we consider ideal edges of the ribbons. The defects of the edge introduce additional intervalley scattering in addition to the adatoms. When the edge is defected, the peaks of conductance for nonzero B change in position and the weak-localization dip varies in depth but the $G(B)$ dependence is not qualitatively changed.

In perpendicular external magnetic field the resonances supported by the adatoms are also associated with current circulation from one scattering event to the other, and the backscattering along the same path which limits the spin-precession effects does not occur [Fig. 10(b)] due to the Lorentz force. This opens a chance for accumulation of the spin-precession effects as for circular n-p junction. High peaks of the spin-flipping contribution to conductance are found [Fig. 14(b)] with irregular positions at the B scale. The peaks of spin-flipping conductance are now correlated with the dips of the spin-conserving conductance in contrast to the results obtained for the circular n-p junction discussed above. The scattering density in the absence of the n-p junction exhibits localization of the quasibound states (Fig. 15) varying between one resonance and the other.

We searched for the relation between the form of the scattering density, the conductance, and its spin-resolved contributions. In Figs. 14(a) and 14(b), the blue line shows the relative contribution of the scattering density at the fluorinated carbon atom and its neighbors to the overall scattering density inside the computational box. In Fig. 14(a), we can see that the transfer probability is minimal when the density localization around the fluorinated carbon atoms is large. On the other hand, the spin-flip transfer probability [Fig. 14(b)] is maximal when the scattering density near the fluorinated atoms is large [Fig. 14(b)]. The results are due to the fact that the fluorine atoms are both sources of backscattering and the spin flips. We found [Fig. 14(c)] a much closer correlation of the spin-flip transfer probability with the ratio of the scattering density

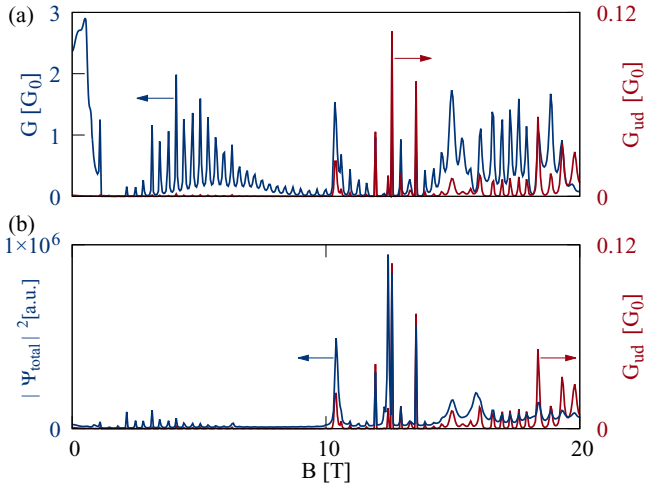

FIG. 16. (a) Conductance (G) and its spin-flipping contribution G_{ud} for a wide nanoribbon with 1017 atoms across and width 125 nm for $E_F = 30$ meV. (b) G_{ud} versus the integral of the wave function within the fluorinated area. Zeeman interaction is neglected.

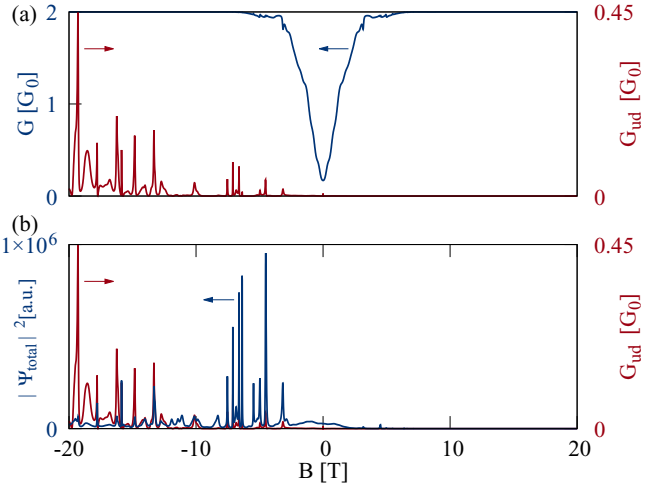

FIG. 18. (a) The conductance G and its spin-flipping contribution G_{ud} for the fluorinated quantum ring of Fig. 3 side attached to the thin channel with 293 atoms across. (b) G_{ud} versus the integral of the scattering wave function within the quantum ring. The spin Zeeman interaction is present. The calculation is for $E_F = 15$ meV and $\eta = 1\%$ concentration of the fluorine atoms with tight-binding parameters taken from [22] for 7×7 supercell.

localized within the entire fluorinated region. In the present approach, the incident electron density is normalized and kept constant for any B. The system of the adatoms for some values of the magnetic field supports a long-living resonance at the Fermi energy. In these conditions, the scattering density within the fluorinated region acquires large values. The integral of the scattering density [Fig. 14(c)] over the fluorinated region reproduces very closely the shape the spin-flip transfer probability as a function of the magnetic field.

E. Wide ribbons and the Zeeman interaction

Formation of the current confinement at the n-p junction or resonances supported by adatoms presented above was due to the orbital effects of the external magnetic field that for the thin ribbon 35 nm wide appeared only for the fields of the order of 50 T. In order to shift the magnetic field scale to lower values, the wider ribbon is needed. The conductance for the fluorinated ribbon of width 125 nm is plotted in Fig. 16(a), still without the Zeeman interaction. The spin flips occur already for B of the order of 10 T and are correlated with formation of localized resonances within the fluorinated ribbon segment [Fig. 16(b)].

All the results presented above were obtained without the spin Zeeman effect. Figure 17 shows the conductance as a function of the external magnetic field with the Zeeman interaction. The peaks of G_{ud} appear but reduced by a factor of $\simeq$10. Similarly, for the n-p junctions induced by external potential, the spin flipping contribution to conductance is drastically reduced by the spin Zeeman interaction. In presence of the spin Zeeman interaction for the perpendicular magnetic field, the electron spin on its motion from one adatom to the other precesses with respect to the z axis. This precession does not change the average $\langle S_z \rangle$ value, only the perpendicular components $\langle S_x \rangle$ and $\langle S_y \rangle$ are affected. The spin-precession length at 10 T is 1.785 μm, i.e., by orders of magnitude larger than the average distance between the F-F adatoms ($\simeq$1.5 nm). The effect behind the reduction of the spin-flipping conductance with the Zeeman interaction is the spin-dependent Fermi wave vector. In the disordered sample, the scattering wave function is very sensitive to the value of the Fermi wave vector and the accumulation of the spin-precession events requires that the electron stays on its path while its spin is rotated. This is no longer the case when the spin Zeeman effect is present. The solution to this problem is given in the next subsection.

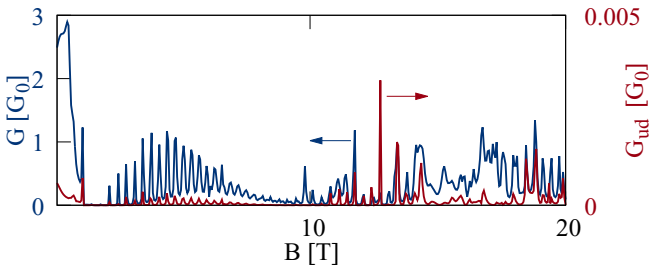

FIG. 17. Same as (a) in presence of the Zeeman interaction.

F. Side-attached quantum rings

A way to keep the electron on its path while the spin is rotated is the application of a lateral confinement of, e.g., quantum ring as in Fig. 3. The quantum ring [45] supports localized resonances with the current circulation of a fixed orientation. The results for the ring attached to the thin ribbon with the Zeeman interaction is given in Fig. 18. The spin-flipping contributions to conductance acquire values in spite of the presence of the spin Zeeman interaction.

The overall conductance is a symmetric function of the external magnetic field $G(B) = G(-B)$ in consistence with the Onsager relation for a two-terminal device. Nevertheless, the spin-flipping contribution to conductance depends on the

orientation of the magnetic field. The spin flips occur only for $B < 0$, i.e., for the magnetic field oriented in the $+z$ direction which injects [45,51] the incident electron wave function from the ribbon to the quantum ring. The injection occurs only provided that a localized resonance is supported by the ring for the applied value of the magnetic field [45]. For strong magnetic field oriented in the $-z$ direction, the electron wave function is kept to the lower edge of the ribbon and does not notice the presence of the ring. This fact, with the Onsager relation, leads to $G(\pm B) = 2G_0$ limit for high magnetic fields inducing the quantum Hall conditions [see Fig. 18(a)].

IV. SUMMARY AND CONCLUSIONS

We studied charge and spin transport across a graphene nanoribbon with dilute concentration of fluorine adatoms using the wave-function-matching technique within the tight-binding approach. The electron passage below a single F adatom induces a small rotation of the electron spin due to the precession by a local Rashba interaction. In order to produce a spin flip, many local precession events at separate adatoms need to accumulate. We demonstrated that the necessary accumulation occurs when the electron circulates around a closed path in localized resonant states supported by a n-p junction or by the adatoms themselves. The accumulation is deteriorated by the spin Zeeman interaction which introduces the spin dependence to the electron trajectory. The dependence is of a secondary importance for a quantum ring side attached to the nanoribbon which supports the localized resonances with a fixed electron circulation around the ring and allows for large spin-flipping contribution to conductance for the magnetic field orientation which injects the incident electron to the ring.

ACKNOWLEDGMENTS

This work was supported by the National Science Centre (NCN) according to decision No. DEC-2015/17/B/ST3/01161. The calculations were performed on PL-Grid Infrastructure.

[1] I. Zutic, J. Fabian, and S. Das Sarma, Rev. Mod. Phys. **76**, 323 (2004).
[2] S. Datta and B. Das, Appl. Phys. Lett. **56**, 665 (1990).
[3] A. H. Castro Neto, F. Guinea, N. M. R. Peres, K. S. Novoselov, and A. K. Geim, Rev. Mod. Phys. **81**, 109 (2009).
[4] W. Han and R. K. Kawakami, Phys. Rev. Lett. **107**, 047207 (2011).
[5] T. Maassen, J. J. van den Berg, N. Ijbema, F. Fromm, T. Seyller, R. Yakimova, and B. J. van Wees, Nano Lett., **12**, 1498 (2012).
[6] A. Manchon, H. C. Koo, J. Nitta, S. M. Frolov, and R. A. Duine, Nat. Mater. **14**, 871 (2015)
[7] E. A. Laird, F. Kuemmeth, G. Steele, K. Grove-Rasmussen, J. Nygård, K. Flensberg, L. P. Kouwenhoven, Rev. Mod. Phys. **87**, 703 (2015).
[8] A. Avsar, J. Y. Tan, T. Taychatanapat, J. Balakrishnan, G. K. W. Koon, Y. Yeo, J. Lahiri, A. Carvalho, A. S. Rodin, E. C. T. O'Farrell *et al.*, Nat. Commun. **5**, 4875 (2014).
[9] M. Gmitra, D. Kochan, P. Högl, and J. Fabian, Phys. Rev. B **93**, 155104 (2016).
[10] V. N. Kotov, B. Uchoa, V. M. Pereira, F. Guinea, and A. H. Castro-Neto, Rev. Mod. Phys. **84**, 1067 (2012).
[11] O. Leenaerts, B. Partoens, and F. M. Peeters, Phys. Rev. B **80**, 245422 (2009).
[12] J. J. Palacios, J. Fernández-Rossier, and L. Brey, Phys. Rev. B **77**, 195428 (2008).
[13] P. Haase, S. Fuchs, T. Pruschke, H. Ochoa, and F. Guinea, Phys. Rev. B **83**, 241408 (2011).
[14] N. A. Pike and D. Stroud, Phys. Rev. B **89**, 115428 (2014).
[15] F. Gargiulo, G. Autès, N. Virk, S. Barthel, M. Rösner, L. R. M. Toller, T. O. Wehling, and O. Yazyev, Phys. Rev. Lett. **113**, 246601 (2014).
[16] J. Zhou, Q. Wang, Q. Sun, X. S. Chen, Y. Kawazoe, and P. Jena, Nano Lett. **9**, 3867 (2009).
[17] M. Sepioni, R. R. Nair, S. Rablen, J. Narayanan, F. Tuna, R. Winpenny, A. K. Geim, and I. V. Grigorieva, Phys. Rev. Lett. **105**, 207205 (2010).
[18] X. Hong, S.-H. Cheng, C. Herding, and J. Zhu, Phys. Rev. B **83**, 085410 (2011).
[19] R. R. Nair, M. Sepioni, I.-L. Tsai, O. Lehtinen, J. Keinonen, A. V. Krasheninnikov, T. Thomson, A. K. Geim, and I. V. Grigorieva, Nat. Phys. **8**, 199 (2012).
[20] X. Hong, K. Zou, B. Wang, S.-H. Cheng, and J. Zhu, Phys. Rev. Lett. **108**, 226602 (2012).
[21] H. Santos and L. Henrard, J. Phys. Chem. C **118**, 27074 (2014).
[22] S. Irmer, T. Frank, S. Putz, M. Gmitra, D. Kochan, and J. Fabian, Phys. Rev. B **91**, 115141 (2015).
[23] R. R. Nair, M. Sepioni, I.-L. Tsai, O. Lehtinen, J. A. A. Stabile, A. Ferreira, J. Li, N. M. R. Peres, and J. Zhu, Phys. Rev. B **92**, 121411(R) (2015).
[24] A. Sadeghi, M. Neek-Amal, G. R. Berdiyorov, and F. M. Peeters, Phys. Rev. B **91**, 014304 (2015).
[25] K. Wakabayashi, Y. Takane, M. Yamamoto, and M. Sigrist, Carbon **47**, 124 (2009).
[26] P. Chuang, S.-C. Ho, L. W. Smith, F. Sfigakis, M. Pepper, C.-H. Chen, J.-C. Fan, J. P. Griffiths, I. Farrer, H. E. Beere *et al.*, Nat. Nanotechnol. **10**, 35 (2015).
[27] D. A. Abanin and L. S. Levitov, Science **317**, 641 (2007).
[28] J. R. Williams, L. DiCarlo, and C. M. Marcus, Science **317**, 638 (2007).
[29] J. Tworzydło, I. Snyman, A. R. Akhmerov, and C. W. J. Beenakker, Phys. Rev. B **76**, 035411 (2007).
[30] J. R. Williams, T. Low, M. S. Lundstrom, and C. M. Marcus, Nat. Nanotechnol. **6**, 222 (2011).
[31] A. Cresti, G. Grosso, and G. P. Parravicini, Phys. Rev. B **77**, 233402 (2008).
[32] T. Taychatanapat, J. Y. Tan, Y. Yeo, K. Watanabe, T. Taniguchi, and B. Özyilmaz, Nat. Commun. **6**, 6093 (2015).
[33] P. Rickhaus, P. Makk, M.-H. Liu, E. Tóvári, M. Weiss, R. Maurand, K. Richter, and C. Schönenberger, Nat. Commun. **6**, 6470 (2015).
[34] K. Kolasiński, A. Mreńca-Kolasińska, and B. Szafran, Phys. Rev. B **95**, 045304 (2017).

[35] J. R. Williams and C. M. Marcus, Phys. Rev. Lett. **107**, 046602 (2011).
[36] P. Carmier, C. Lewenkopf, and D. Ullmo, Phys. Rev. B **84**, 195428 (2011).
[37] M. Barbier, G. Papp, and F. M. Peeters, Appl. Phys. Lett. **100**, 163121 (2012); S. P. Milovanović, M. Ramezani Masir, and F. M. Peeters, *ibid.* **105**, 123507 (2014).
[38] N. Davies, A. A. Patel, A. Cortijo, V. Cheianov, F. Guinea, and V. I. Fal'ko, Phys. Rev. B **85**, 155433 (2012).
[39] J.-C. Chen, X. C. Xie, and Q.-F. Sun, Phys. Rev. B **86**, 035429 (2012).
[40] Y. Liu, R. P. Tiwari, M. Brada, C. Bruder, F. V. Kusmartsev, and E. J. Mele, Phys. Rev. B **92**, 235438 (2015).
[41] T. Taychatanapat, K. Watanabe, T. Taniguchi, and P. Jarillo-Herrero, Nat. Phys. **9**, 225 (2013).
[42] S. Bhandari, G.-H. Lee, A. Klales, K. Watanabe, T. Taniguchi, E. Heller, P. Kim, and R. M. Westervelt, Nano Lett. **16**, 1690 (2016).
[43] M.-H. Liu, C. Gorini, and K. Richter, Phys. Rev. Lett. **118**, 066801 (2017).
[44] A. Mreńca-Kolasińska, S. Heun, and B. Szafran, Phys. Rev. B **93**, 125411 (2016).
[45] A. Mreńca-Kolasińska and B. Szafran, Phys. Rev. B **94**, 195315 (2016).
[46] F. V. Tikhonenko, D. W. Horsell, R. V. Gorbachev, and A. K. Savchenko, Phys. Rev. Lett. **100**, 056802 (2008).
[47] D. Cabosart, S. Faniel, F. Martins, B. Brun, A. Felten, V. Bayot, and B. Hackens, Phys. Rev. B **90**, 205433 (2014).
[48] S. Russo, J. B. Oostinga, D. Wehenkel, H. B. Heersche, S. S. Sobhani, L. M. K. Vandersypen, and A. F. Morpurgo, Phys. Rev. B **77**, 085413 (2008).
[49] D. Smirnov, J. C. Rode, and R. J. Haug, Appl. Phys. Lett. **105**, 082112 (2014).
[50] M. Huefner, F. Molitor, A. Jacobsen, A. Pioda, C. Stampfer, K. Ensslin, and T. Ihn, New J. Phys. **12**, 043054 (2010).
[51] J. Dauber, M. Oellers, F. Venn, A. Epping, K. Watanabe, T. Taniguchi, F. Hassler, and C. Stampfer, Phys. Rev. B **96**, 205407 (2017).
[52] M. Y. Han, B. Ozyilmaz, Y. B. Zhang, and P. Kim, Phys. Rev. Lett. **98**, 206805 (2007).
[53] Z. H. Chen, Y. M. Lin, M. J. Rooks, and P. Avouris, Phys. E **40**, 228 (2007).
[54] M. Evaldsson, I. V. Zozoulenko, H. Xu, and T. Heinzel, Phys. Rev. B **78**, 161407(R) (2008).
[55] T. O. Wehling, M. I. Katsnelson, and A. I. Lichtenstein, Phys. Rev. B **80**, 085428 (2009).
[56] R. M. Guzmán-Arellano, A. D. Hernández-Nieves, C. A. Balseiro, and G. Usaj, Appl. Phys. Lett. **105**, 121606 (2014).
[57] C. L. Kane and E. J. Mele, Phys. Rev. Lett. **95**, 226801 (2005).
[58] C.-C. Liu, H. Jiang, and Y. Yao, Phys. Rev. B **84**, 195430 (2011).
[59] K. Kolasiński and B. Szafran, Phys. Rev. B **88**, 165306 (2013).
[60] M. Zwierzycki, P. A. Khomyakov, A. A. Starikov, K. Xia, M. Talanana, P. X. Xu, V. M. Karpan, I. Marushchenko, I. Turek, G. E. W. Bauer *et al.*, Phys. Status Solidi B **245**, 623 (2008).
[61] C. Pacher, C. Rauch, G. Strasser, E. Gornik, F. Elsholz, A. Wacker, G. Kiesslich, and E. Schöll, Appl. Phys. Lett. **79**, 1486 (2001).
[62] L. Meier, G. Salis, I. Shorubalko, E. Gini, S. Schön, and K. Ensslin, Nat. Phys. **3**, 650 (2007).
[63] S. Bednarek and B. Szafran, Phys. Rev. Lett. **101**, 216805 (2008).